

Morphodynamic modelling of beach cusp formation: the role of wave forcing and sediment composition

Christopher J. Daly^{a,b,*}, France Floc'h^b, Luis P.M. Almeida^c, Rafael Almar^a, Marion Jaud^b

^a*LEGOS, IRD, 31400 Toulouse, France*

^b*University of Brest, CNRS, IUEM, UMR 6538 Géosciences Océan, 29290 Plouzané, France*

^c*Universidade Federal do Rio Grande, Rio Grande do Sul, Brazil*

Abstract

A field of beach cusps formed during a field experiment at Nha Trang Beach, Vietnam, under accretive conditions. The measured data was used to set-up morphodynamic simulations in XBeach, which was able to simulate cusp formation from an initially long-shore uniform beach profile. Several types of simulations were run in order to observe the resulting variation in mean cusp dimensions (length, depth and height), swash flow patterns, and sediment sorting. Both time-constant (JONSWAP) and time-varying (measured) wave forcing conditions were superimposed on the measured tide. In the former, four wave parameters were varied (wave height, period, direction, and spreading), while in the latter, the median sediment size and sediment composition were varied. The wave period was found to primarily influence long-shore length scales, the wave height cross-shore length scales, and obliquely incident waves enhance all these dimensions particularly under narrow-banded conditions. Cusps are not prominent if the wave energy is too low to effect

*Corresponding Author: christopher.daly@legos.obs-mip.fr

significant onshore transport, if the wave angle of incidence and spreading are too large (effectively smoothing out swash perturbations), or if the sediment is too fine in relation to the wave conditions (dissipative beaches or highly erosive wave conditions). Coarse sediment generally tends to be located on cusp horns above the waterline, but is otherwise variable depending on cross-shore location and tide levels. As the XBeach model results show large agreement with well-established norms, it may therefore be used to more rigorously study processes that help to initiate cusps in future work.

Keywords: Beach cusps, Onshore sediment transport, Pattern formation, Wave forcing, Sediment sorting

1 1. Introduction

2 Rhythmic cusped features are commonly observed on sandy beaches with
3 wavelengths up to ~ 1 km. Of these, those with long-shore wavelengths (spac-
4 ing) up to ~ 50 m are usually considered to be formed under swash-dominant
5 processes. Numerous field studies have repeatedly shown that beach cusps
6 generally form during calm, narrow-banded, shore-normal wave conditions
7 which promote accretion (Holland, 1998; Almar et al., 2008; Vourdoukas,
8 2012; O’Dea and Brodie, 2019). Cusps also form (less frequently) under en-
9 ergetic or erosive conditions, and their morphological development is often
10 dynamic, featuring long-shore migration in which new cusp fields are gen-
11 erated over pre-existing formations (Masselink et al., 1997; Masselink and
12 Pattiaratchi, 1998b; van Gaalen et al., 2011). The presence of cusps depends
13 on local characteristics such as sediment size, beach slope and wave energy
14 (van Gaalen et al., 2011), with cusps being more prevalent on steep, coarse

15 grained, reflective beaches. Cusps are frequently characterised by their spac-
16 ing, which is thought to be determined by the wavelength of edge waves
17 (Guza and Inman, 1975) or a function of the swash excursion (Coco et al.,
18 2001; Sunamura, 2004).

19 Cusps are often thought to develop via two primary mechanisms: 1) wave
20 height patterns caused by edge waves in the long-shore dimension (Inman and
21 Guza, 1982), or 2) from self-organisation which allows small bathymetric per-
22 turbations to grow through positive morphodynamic feedback mechanisms
23 (Werner and Fink, 1993; Coco et al., 1999). Whether or not edge waves,
24 self organisation, or a combination of both theories are responsible for beach
25 cusp formation remains an open question (Holland and Holman, 1996; O’Dea
26 and Brodie, 2019). Recent numerical simulations of nearshore flow patterns
27 suggest that wave reflection over steep beaches can also be a mechanism for
28 beach cusp formation (Almar et al., 2018). While much research, based on
29 these pioneering works, has been focused on the question of how cusps are ini-
30 tiated, it is also important to understand how they evolve once formed under
31 varying wave conditions and beach types (Holland, 1998; van Gaalen et al.,
32 2011). Furthermore, while most of what is known about cusp development
33 is based on field observations, numerical simulations have provided valuable
34 insight into how cusps are formed (Werner and Fink, 1993; Coco et al., 2000),
35 what processes are important for their development (Dodd et al., 2008), how
36 their geometry affects swash flow patterns (Masselink et al., 1997), and how
37 surf zone circulation affects cusp development (Garnier et al., 2010). Nu-
38 merical simulations may therefore be used to glean knowledge on how cusps
39 respond to changes in wave forcing and sediment composition, and to predict

40 cusp morphology for specific locations.

41 Numerical simulations of cusp development often require specialized mod-
42 els capable of resolving swash dynamics and processes such as short wave
43 runup, swash sediment transport, and groundwater infiltration and exfiltra-
44 tion (Coco et al., 2000, 2003; Dodd et al., 2008). It is also important to
45 consider other processes such as sediment exchange between the swash and
46 surf zone, wave-wave (bore) interactions and turbulence, and infragravity
47 wave runup (Bakhtyar et al., 2009). Coco et al. (2000) and Dodd et al.
48 (2008) used a process-based modelling approach to allow cusps to form from
49 an initially long-shore uniform beach profile, in which sediment was reworked
50 in the swash. As these simulations were initiated at the base of the swash,
51 surf zone processes were not included. On the other hand, Garnier et al.
52 (2010) excludes swash zone processes from their simulations, which showed
53 that inner surf zone processes may enhance cusp development higher up on
54 the beachface. Using established morphodynamic nearshore models, such as
55 XBeach (Roelvink et al., 2009), one can simulate the entire range from surf
56 to swash including processes important in the development of cusps.

57 The Kingsday version of XBeach (Roelvink et al., 2015) includes a wave-
58 resolving (non-hydrostatic) model, similar to a one-layer implementation of
59 SWASH (Zijlema et al., 2011), and an underlying surfbeat model which allows
60 both short and infragravity waves to be resolved in the swash. Several studies
61 have shown the applicability of the SWASH and XBeach models to simulate
62 wave runup, infragravity motions, swash hydrodynamics and nearshore cir-
63 culation (de Bakker et al., 2014; Lashley et al., 2018; Almar et al., 2018;
64 Roelvink et al., 2018). While the coupling of the sediment transport module

65 with the non-hydrostatic wave solver is still under development, it has been
66 used experimentally in Daly et al. (2017) and Ruffini et al. (2020). In partic-
67 ular, Daly et al. (2017) showed that it is possible to simulate beach accretion
68 and berm formation in XBeach, a key process in the development of cusps.

69 Here, we use the XBeach model to expand the work of Daly et al. (2017)
70 from a 1D to a 2D domain in order to simulate beach cusp formation and
71 evolution under varying wave forcing conditions and sediment composition.
72 The model is benchmarked using data observed during a field campaign at
73 Nha Trang Beach, Vietnam, in November 2015, during which beach cusps
74 formed quickly during an accretionary stage lasting for a few days. We aim to
75 evaluate the performance of the model by comparing predicted length scales,
76 sediment sorting, and swash circulation patterns to what is expected based on
77 observations at Nha Trang Beach and that presented in the literature. Based
78 on the evaluation of the model performance, more detailed investigation into
79 key processes that influence cusp initiation may be carried out in future work.

80 **2. Methods**

81 *2.1. Location and Measured Data*

82 An 8-day field experiment was performed at Nha Trang beach, Vietnam,
83 from 27 November to 4 December 2015 ($12^{\circ} 15.17'$ N, $109^{\circ} 11.81'$ E, Fig.
84 1). A 1200 kHz acoustic Doppler current profiler (ADCP) placed offshore
85 at 15 m depth measured significant wave heights varying between 0.6 and
86 1.5 m, and mean wave periods varying between 7 and 12 s (Fig. 2a). Wave
87 transformation along an instrumented cross-shore transect in the surf and
88 swash zone were measured using four pressure transducers. A 25 Hz SICK

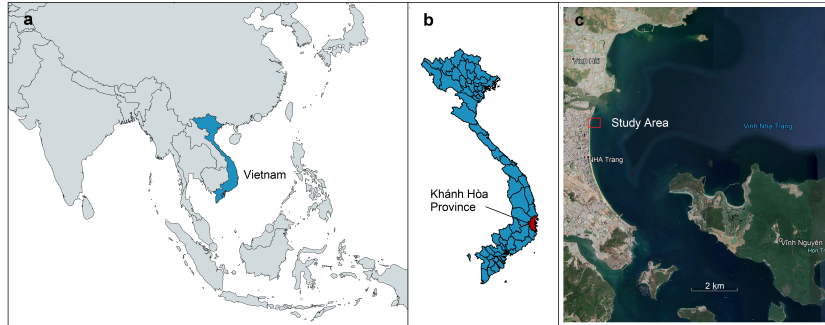


Figure 1: Location of the Nha Trang beach study site (red box in panel c), in the Khánh Hòa Province (red area in panel b), of Vietnam, southeast Asia (blue area in panel a).

89 LMS511 2D laser scanner was used to measure surface elevation (both of
 90 the bed and water) in the swash along the same transect, from which the
 91 swash excursion, swash height and beach slope is determined (Fig. 2c–d).
 92 The beach is composed of coarse grained sediment (median grain size, D_{50}
 93 = 0.5 mm) and is located in a diurnal, micro-tidal environment (tide range
 94 = 1.6 m). As a result, the beach has a fairly steep (1:8) swash slope and a
 95 narrow low tide terrace. Beach topography data was measured using high-
 96 resolution drone photogrammetry (output resolution of data points being
 97 2.85 cm) and closely spaced (~ 10 m) RTK-GPS transects over a 1 km length
 98 of beach, centered on the instrumented cross-shore transect. The surveys
 99 were carried out daily and captured the rapid formation of accretionary beach
 100 cusps between 28 November and 1 December (Fig. 3). Based on these
 101 measurements, the cusps had a mean spacing of approximately 28 m. Further
 102 details of the setup of the field experiment are presented in Almeida et al.
 103 (2020) and Daly et al. (2017).

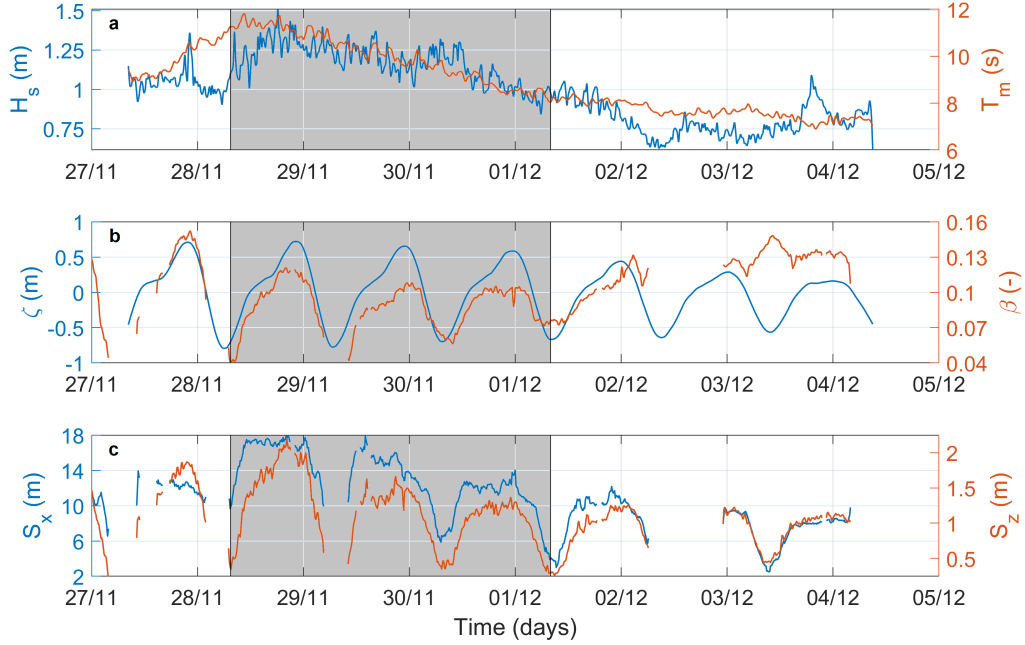


Figure 2: Wave conditions measured at the offshore ADCP and swash geometry measured with LIDAR at Nha Trang during the 2015 field experiment. (Panel a) significant wave height, H_s , and mean wave period, T_m . (Panel b) tide elevation, ζ , and beach slope, β . (Panel c) swash excursion, S_x , and swash height, S_z . The three-day simulation period for Series C is highlighted in grey.

104 *2.2. Numerical Model*

105 *2.2.1. Model Description*

106 The Kingsday version of XBeach (cf. XBeach user manual, (Roelvink
 107 et al., 2015)) is used here with the non-hydrostatic wave solver (fully wave-
 108 resolving) enabled, rather than the default surf-beat mode (wave-group-
 109 resolving). The non-hydrostatic mode gives a better representation of waves
 110 in the swash zone by combining both short and infragravity parts of the wave
 111 spectrum, albeit at the expense of having to use a much more highly resolved

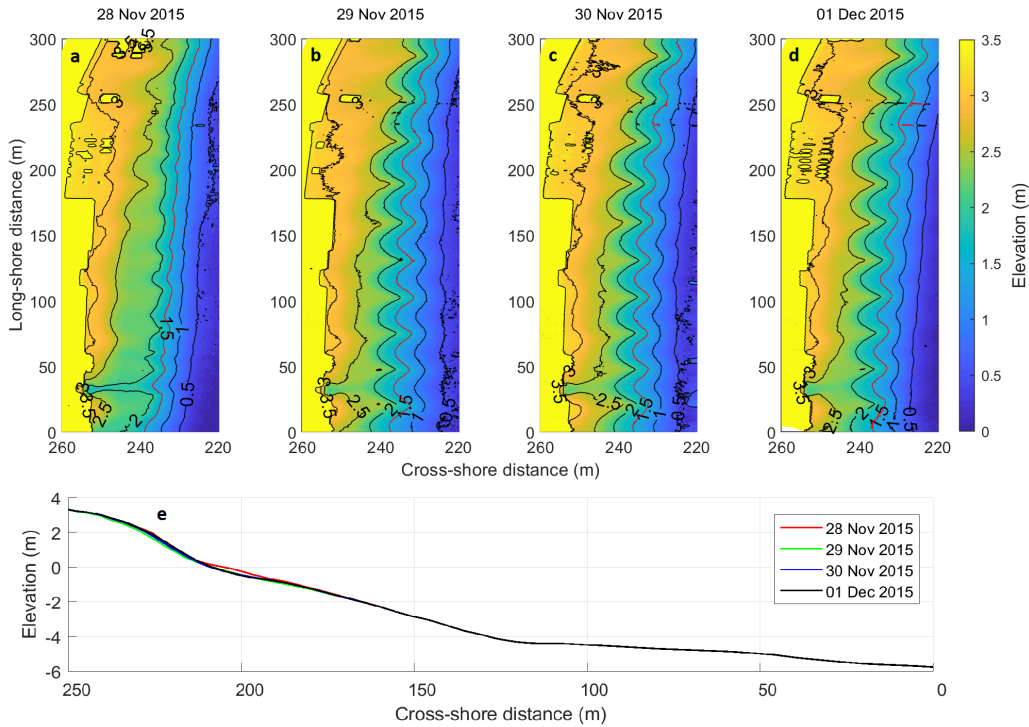


Figure 3: (Panels a-d) Measured elevations at Nha Trang during the field experiment from drone photogrammetry. Changes in morphology show the emergence of beach cusps over 3 days from 28 November (top left) to 1 December (top right), 2015. (Panel e) Long-shore-averaged cross-shore profile of the measured bathymetry.

112 computational grid. In non-hydrostatic mode, short-wave non-linearity is im-
 113 plicitly accounted for in the flow velocity at the bed, without the need for
 114 corrections based on estimates of asymmetry and skewness (e.g. Ruessink
 115 et al. (2012)). Sediment transport is computed based on mean flow conditions
 116 averaged over the wave period using advection-diffusion equations, where the
 117 Eulerian flow velocity is applied to the bed and suspended load transport for-
 118 mulations of Soulsby (1997), van Rijn (2007a) and van Rijn (2007b). Mean
 119 cross-shore flow (and thus, bed-load transport) tends to be negative (offshore-

120 directed), driven by undertow (van der Werf et al., 2017). In nature this is
121 can be effectively counter-balanced by non-linear wave-induced accelerations
122 which promote net onshore transport, resulting in accretion (Elgar et al.,
123 2001). Such intra-wave accelerations are not yet accounted for in XBeach
124 non-hydrostatic mode as sediment transport calculations are wave-averaged,
125 resulting in a tendency for the model to over-predict erosion. However, Daly
126 et al. (2017) produced simulations of Nha Trang which allowed accretion of
127 the beach. This rather unexpected result was found by using a combination
128 of parameter settings which essentially modified the bed load transport di-
129 rection in shallow water such that it is constantly positive (onshore-directed).
130 Suspended load transport, however, is not affected, and can be both positive
131 or negative. Therefore, although XBeach may be run with default parameter
132 settings, some modifications are required for simulating swash morphody-
133 namics, discussed following.

134 *2.2.2. Modified Parameter Settings and Prior Validation*

135 Identical parameter settings are used in the current suite of simulations
136 as presented in Daly et al. (2017), shown in Table 1 below. Four groups of
137 model parameters are changed from their default setting, relating to 1) bed
138 friction (*bedfriction* and *bedfriccoef*), 2) bed slope effects (*facsl* and *bdslop-*
139 *effdir*), 3) hindered erosion (*dilatancy*), and 4) groundwater flow (*gwflow*,
140 *gw0*, *kx/ky/kz* and *gwhorinfil*). A detailed description of the role each group
141 of parameters play in achieving onshore transport is given in Daly et al.
142 (2017), and mentioned briefly here. 1) The Manning bed friction model is
143 used as it assigns higher friction values to shallow depths than Chézy (de-
144 fault model), thereby slightly damping flow velocities and allowing increased

145 sediment settling and berm formation in the upper swash. 2) The parame-
 146 ters controlling bed slope effects modify the direction and magnitude of bed
 147 load transport based on the bed slope (cf. Walstra et al. (2007)) using the
 148 model of Talmon et al. (1995). 3) Dilatancy effects hinder erosion under
 149 high swash flows as under-pressure in the bed reduces water inflow, making
 150 it more difficult for sediment to become entrained. Dilatancy is accounted for
 151 by limiting the critical Shields number (cf. van Rhee (2010)). Finally, 4) the
 152 groundwater flow module allows water infiltration (exfiltration) into (from)
 153 the bed. Infiltration in the upper swash allows sediment deposits to build
 154 up and form berms, and is therefore a critical process in simulating swash
 155 morphodynamics. Groundwater is modelled using Darcy flow equations (cf.
 156 McCall et al. (2012)), and depends on the permeability of the sediment.

Keyword	Function	Value
<i>bedfriction</i>	Bed friction formulation	Manning
<i>bedfriccoef</i>	Bed friction coefficient	0.02
<i>facsl</i>	Bed slope effect factor	0.15
<i>bdslopeffdir</i>	Modify sediment transport direction	Talmon
<i>dilatancy</i>	Turn on/off dilatancy	1 (on)
<i>gwflow</i>	Turn on/off groundwater flow	1 (on)
<i>gw0</i>	Groundwater level	0.28 m
<i>kx/ky/kz</i>	Darcy flow permeability coefficient	0.001
<i>gwhorinfil</i>	Turn on/off horizontal infiltration	1 (on)

Table 1: XBeach model settings changed from default

157 The modified model settings in Table 1 have been validated for the lo-
 158 cation at Nha Trang Beach in Daly et al. (2017). Their simulations were
 159 done over the 1-dimensional long-shore-averaged beach profile starting on 27

160 November 2015 and run for 6 days. Comparisons between the model output
161 and measured H_s data at several locations in the inner surf and swash zone
162 had an average root-mean-square error of 0.15 m and correlation coefficient
163 of 0.94. Furthermore, comparison between the simulated and measured mean
164 cross-shore profile showed a root-mean-square error of 0.11 m. Those results
165 showed that the model reproduces wave transformation up to the swash zone
166 quite well, and also reasonably predicts berm formation on the upper beach.
167 Further validation of the model is therefore not necessary here, as the focus
168 of the study now shifts to assessing the effect varying wave conditions and
169 sediment composition has on cusp formation.

170 *2.3. Numerical Simulations*

171 *2.3.1. Model Grid and Timing*

172 The mean cross-shore profile of the study area on 28 November is used to
173 create a long-shore uniform initial bathymetry for the model (Fig. 3e). When
174 using the non-hydrostatic wave mode in XBeach, a detailed computational
175 grid is required. As such, a grid spacing of 0.75 and 1.5 m in the cross-shore
176 and long-shore directions are used in the surf and swash zone (area above
177 2 m depth), respectively. Initial tests with a finer cross-shore grid spacing
178 of 0.5 m did not significantly change the final result. At the offshore model
179 boundary, the water depth is 6 m and a maximum cross-shore spacing of 2 m
180 is used, which gradually decreases toward the resolution used in the surf and
181 swash zone. The grid spacing used allows waves down to 3 s to be clearly
182 resolved across the entire domain with a minimum 8 points per wavelength
183 (and 16 points per wavelength for periods over 7 s). The high resolution grid
184 in the surf and swash zone also allows beach cusps with wavelengths upwards

185 of 12 m to be adequately resolved.

186 All simulations are run for a period of three days, representing the period
187 during which cusps formed during the field experiment between 28 November
188 and 1 December, 2015, (Fig. 3). The three day period is expected to be
189 sufficient time for cusps to fully form in the model, given that it took only one
190 day for them to emerge during the field experiment. As the computational
191 effort for each simulation is expensive, a modest morphological acceleration
192 factor (*morfac*) of 6 is used to speed up the simulations. Comparable results
193 were obtained for test simulations run with *morfac* turned on and off. The
194 model determines the time step based on a prescribed maximum Courant
195 number (0.7 by default).

196 The output model domain is limited to a dedicated 240×250 m area in
197 the long-shore (y) and cross-shore (x) dimensions, respectively. This area is
198 sufficient to observe the development of cusps with long-shore wavelengths up
199 to 60 m (minimum 4 wavelengths within the domain). A buffer area is added
200 at either end of the output model domain to account for boundary effects,
201 especially in cases where waves approach the beach at an oblique angle and
202 create shadow zones. This area is removed during the post-processing of
203 the results. In order to limit the size of the output files, time-averaged and
204 instantaneous global variables (i.e. 2-dimensional) are saved every 10 minutes
205 (e.g. bed levels, surface elevation, velocity and bed composition). A more
206 highly resolved time series is saved every 0.5 s for output variables at several
207 points along the central cross-shore transect (at $y = 120$ m).

208 *2.3.2. Wave Conditions and Sediment Composition*

209 Simulations are run using either time-constant or time-varying (measured) wave forcing conditions. All simulations are run with the same time-varying (measured) diurnal tidal water levels imposed on the model boundary. For simulations with time-constant wave forcing, a random time-series of surface waves are generated using a JONSWAP spectrum defined by four parameters: the significant wave height (H_s), mean wave period (T_m), directional spreading (σ), and angle of incidence (θ). The values of H_s and T_m fall within close range of the measured conditions during the field experiment (cf. Fig. 2). A *base case* simulation uses $[H_s, T_m, \sigma, \theta] = [1.3 \text{ m}, 10 \text{ s}, 0^\circ, 0^\circ]$. From this simulation, each parameter is varied with values shown in Table 2 below. The 2-dimensional H_s - T_m parameter space is completely filled with the exception that at $H_s = 0.7 \text{ m}$ there is no simulation at $T_m = 11.4 \text{ s}$, and at $H_s = 1.7 \text{ m}$ there is no simulation at $T_m = 7.3 \text{ s}$, as these wave conditions are far from those observed. The parameter space for σ and θ is 1-dimensional. There are 14 time-constant wave simulations for the H_s - T_m parameter space (Series A1 – A14, including the *base case* at A10), and 6 other simulations for the σ and θ parameter space (Series B1 – B6).

Wave Parameter	Values Used
H_s (m)	[0.7, 1.0, 1.3, 1.7]
T_m (s)	[7.3, 8.7, 10.0, 11.4]
σ ($^\circ$)	[0, 5, 10, 15]
θ ($^\circ$)	[0, 5, 10, 15]

Table 2: Wave parameter values used to define JONSWAP boundary wave conditions

226 Simulations using time-varying (measured) wave conditions directly use

227 the time-series of wave conditions recorded by the offshore ADCP during the
 228 field campaign (cf. Fig. 2). The wave direction is, however, kept constant
 229 at 0 ° (normally incident). The median grain size, D_{50} , is varied in these
 230 simulations as [0.5, 0.3, 0.2, 0.5/0.2] mm (Series C1 – C4, respectively).
 231 The first (0.5 mm) represents the native size of sediment of the beach while
 232 the other sizes are exploratory. The latter size (0.5/0.2 mm) features an
 233 evenly mixed sediment bed of coarse and fine sediment, respectively.

234 *2.3.3. Analysis of Results*

235 Contour lines are extracted from output bed level data between -1.5 and
 236 2.5 m elevation at 0.1 m intervals. The spatial dimensions of the beach cusps
 237 produced during the simulations are determined by Fourier analysis of each
 238 contour level at each point in time, yielding the mean long-shore wavelength
 239 (or cusp spacing, L_y) and cross-shore depth (L_x). Similarly, the vertical
 240 height (L_z) of the cusps are derived from the analysis of the detrended long-
 241 shore bed level at each cross-shore location. Variation of the bathymetry (z_b)
 242 in the long-shore dimension is computed by removing the long-shore mean
 243 profile from each cross-shore transect:

$$\widetilde{z}_{b,y} = z_b - \overline{z_{b,y}} \quad (1)$$

244 Subsequently, the root-mean-square (RMS) long-shore bed level variation
 245 (Δ), which indicates the degree of vertical variability in bed levels and thus
 246 prominence of the cusped features, is computed as:

$$\Delta = \sqrt{\sum_{z_b=0.5}^{z_b=1.0} \widetilde{z}_{b,y}^2} \quad (2)$$

247 Only data located between 0.5 and 1 m elevation are used Eq. 2, an area in
 248 which cusp features are consistently located for all simulations. Beach cusps
 249 are considered to be present if $\Delta > 2$ cm, $L_z > 5$ cm and the aspect ratio
 250 ($AR = L_y/L_x$) < 25 . They are also considered to be prominent if $\Delta > 10$
 251 cm, $L_z > 20$ cm and $AR < 10$.

252 Long-shore variation (or anomaly) of the time-averaged (over a 10 minute
 253 period) significant wave height and cross-shore current (u) field over the
 254 model domain ($\langle \widetilde{H_{s,y}} \rangle$ and $\langle \widetilde{u_y} \rangle$, respectively) are also computed in a similar
 255 fashion as $\widetilde{z_{b,y}}$ in Eq. 1. Turbulent kinetic energy (k) is computed from the
 256 time series output of cross-shore and long-shore velocity components (u and
 257 v , respectively) along the central cross-shore transect as:

$$k = \frac{1}{2} \left(\overline{(u')^2} + \overline{(v')^2} \right) \quad (3)$$

258 where u' and v' are fluctuations of the velocity components after removal of
 259 the mean over a sample period of 10 minutes.

260 The swash excursion (S_x) is computed along the central cross-shore swash
 261 profile (at $y = 120$ m), where water and bed level data are stored at high
 262 frequency (2 Hz) and at 1 m intervals. S_x is taken as the difference between
 263 the cross-shore position of the lower and upper level of the wet/dry interface
 264 (at the 2nd and 98th percentiles, respectively) during successive 10-minute
 265 intervals (n.b., a grid point is considered dry once $h < 5$ cm). The swash
 266 height (S_z) is the corresponding difference between the lower and upper el-
 267 evation of the wet/dry interface during the same time interval. The swash
 268 slope (β) is equal to S_z/S_x .

269 Finally, the surface sediment composition, $P_{D_{50}}$ is computed for case C4

270 (having a mixed sediment bed) as:

$$P_{D_{50}} = \frac{P_{c,t} - P_{c,i}}{P_{c,i}} \quad (4)$$

271 where P_c is the percentage of coarse sediment in the surface layer initially
272 (subscript i , and where $P_{c,i} = 50\%$) or at any time during the simulation
273 (subscript t). Thus, $P_{D_{50}}$ values of 1, 0 and -1 indicate that the surface
274 sediment is 100% coarse, evenly mixed (50% coarse and 50% fine) and 100%
275 fine, respectively.

276 3. Results

277 3.1. Predicted Length Scales

278 The final bathymetries for all 24 simulations (taken at the last mid-tide
279 level at 2.83 days) are shown in Fig. 4. The 14 simulations in Series A are
280 shown in Fig. 4a–n, the 6 simulations in Series B are shown in Fig. 4o–t,
281 and finally, the 4 simulations in Series C are shown in Fig. 4u–x. Here, it is
282 seen that cusps clearly develop for certain cases and are subdued for others.
283 For the cases where cusps do form, they are generally located in a narrow
284 area between 0 and 1.5 m elevation on the sub-aerial beach face. Prominent
285 cusps are obtained for cases A10-14, B1, B4 and C1.

286 The length scales of the cusps vary as they evolve, depending on the eleva-
287 tion of the tide and the movement of the swash zone up and down the beach
288 face, as shown for the *base case* (A10) in Fig. 5. Cusps generally begin to
289 appear after the first tidal cycle with low Δ values, which are then enhanced
290 over the remaining two tidal cycles. At the end of the simulations, the level

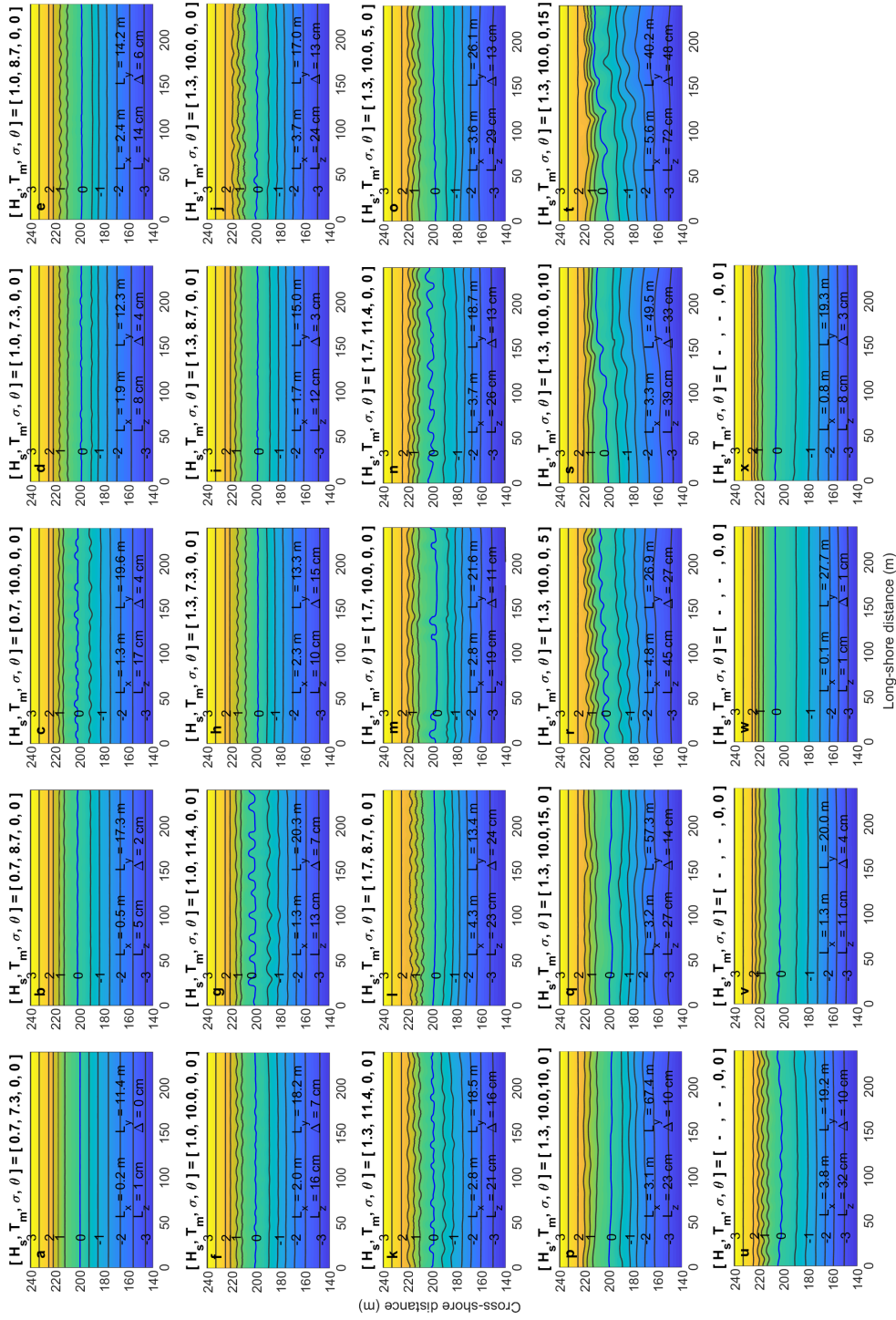


Figure 4: Bathymetry of the model domain extracted at the last mid-tide of the simulation ($T = 2.83$ days) showing resulting cusped features and corresponding length scales. Panels a–t show results for simulations forced with synthetic wave conditions and u–x show those forced with actual wave data while varying D_{50} .

291 of the tide is low, leaving the upper beach exposed and morphologically inac-
292 tive. It is at this moment (mid-tide occurring at 2.83 days) that final values
293 of L_x , L_y , L_z , Δ and AR are taken as representative of the response to the
294 prescribed forcing conditions or sediment composition.

295 3.1.1. Series A: Varying H_s and T_m

296 Fig. 4a–n shows prominent cusps develop for certain combinations of
297 H_s - T_m (generally when $H_s > 1.3$ m and $T_m > 10$ s) and are subdued for
298 others (generally when $H_s < 1$ m and $T_m < 10$ s). There is one case where
299 beach cusps do not form at all (case A1), despite accretion of the beach face.
300 Fig. 6a–d shows the resulting length scales for the simulations in Series A.
301 For cases where cusps are present (A2 – A14), L_y varies between 12 – 22 m.
302 Increases in T_m (for the same H_s) generally results in increased L_y (warmer
303 colours concentrated in top half of Fig. 6b). L_x and L_z increases with
304 increasing H_s and, to a lesser extent, with T_m (warmer colours concentrated
305 in the top right of Fig. 6a and c). And finally, increased Δ values are
306 generally associated with larger H_s (warmer colours concentrated on right
307 side of Fig. 6d).

308 3.1.2. Series B: Varying σ and θ

309 Fig. 6e–h shows the response values of cusp length scales to changes in
310 σ and θ . Increasing values of σ and θ from 0 produce large increases in L_y ,
311 with values ranging between 26 – 67 m. This is a significant increase in L_y
312 compared to the base case, where L_y is 17 m. This may be explained by the
313 increased width of the swash trajectory (i.e. the path a water particle traces
314 during swash and backwash, distinct from S_x) for higher values of σ and θ .

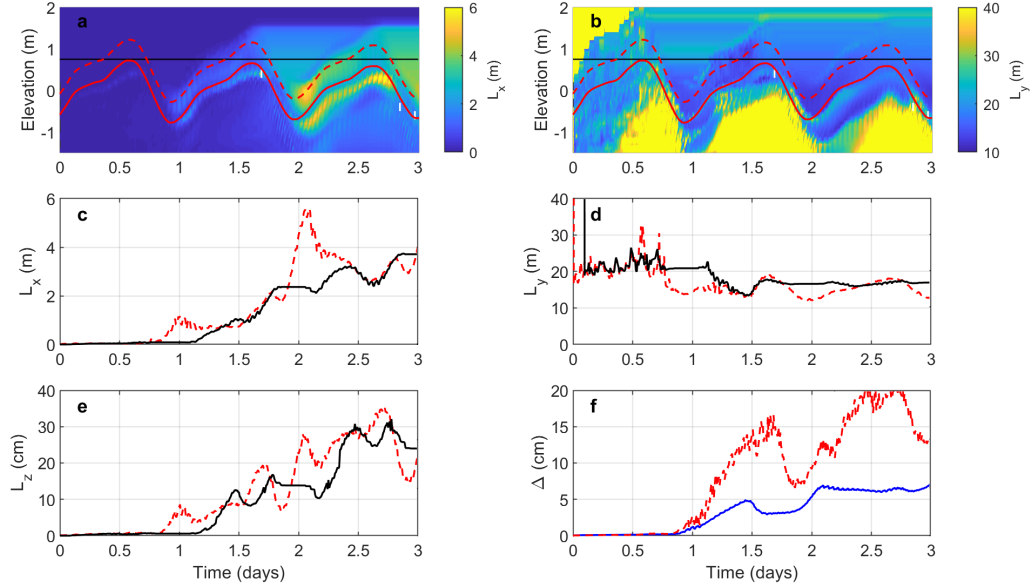


Figure 5: Evolution of beach cusp length scales for the base case simulation. (a–b) Variation of L_x (a) and L_y (b) as a function of time and elevation relative to MSL. The solid red line indicates the height of the tide (near the lower limit of the swash) and the dashed red line shows (approximately) the upper limit of the swash at 0.5 m above the tide level. The solid black line shows the maximum tide level of 0.75 m elevation. Changes in L_x and L_y occur as the swash zone moves up and down the beach face. At low tide (at time = 1, 2 and 3 days), the upper beach is dry and morphologically inactive. (c–f) Changes in L_x , L_y , L_z and Δ as a function of time, respectively. The dashed red line and solid black lines correspond to those defined in (a–b). The solid blue line in (f) is the average Δ taken between 0.5 and 1 m elevation. L_x , L_z and Δ remain low during the first tidal cycle as the planar beach begins to react to the imposed forcing conditions. They subsequently increase over the remaining two tidal cycles.

Run ID	H_s (m)	T_m (s)	σ (°)	θ (°)	D_{50} (mm)	L_x (m)	L_y (m)	L_z (cm)	Δ (cm)	AR (-)
A1	0.7	7.3	0	0	0.5	0.2	11.4	1	0	57
A2	0.7	8.7	0	0	0.5	0.5	17.3	5	2	35
A3	0.7	10.0	0	0	0.5	1.3	19.6	17	4	15
A4	1.0	7.3	0	0	0.5	1.9	12.3	8	4	6.5
A5	1.0	8.7	0	0	0.5	2.4	14.2	14	6	5.9
A6	1.0	10.0	0	0	0.5	2.0	18.2	16	7	9.1
A7	1.0	11.4	0	0	0.5	1.3	20.3	13	7	16
A8	1.3	7.3	0	0	0.5	2.3	13.3	10	15	5.8
A9	1.3	8.7	0	0	0.5	1.7	15.0	12	3	8.8
A10	1.3	10.0	0	0	0.5	3.7	17.0	24	13	4.6
A11	1.3	11.4	0	0	0.5	2.8	18.5	21	16	6.6
A12	1.7	8.7	0	0	0.5	4.3	13.4	23	24	3.1
A13	1.7	10.0	0	0	0.5	2.8	21.6	19	11	7.5
A14	1.7	11.4	0	0	0.5	3.7	18.7	26	13	5.1
B1	1.3	10.0	5	0	0.5	3.6	26.1	29	13	7.3
B2	1.3	10.0	10	0	0.5	3.1	67.4	23	10	22
B3	1.3	10.0	15	0	0.5	3.2	57.3	27	14	18
B4	1.3	10.0	0	5	0.5	4.8	26.9	45	27	5.6
B5	1.3	10.0	0	10	0.5	3.3	49.5	39	33	15
B6	1.3	10.0	0	15	0.5	5.6	40.2	72	48	17
C1	varies	varies	0	0	0.5	3.8	19.2	32	10	5.1
C2	varies	varies	0	0	0.3	1.3	20.0	11	4	15
C3	varies	varies	0	0	0.2	0.1	27.7	1	1	277
C4	varies	varies	0	0	0.5/0.2	0.8	19.3	8	3	24

Table 3: Simulation Results (base case in bold)

315 It is important to also note in Fig. 4 that for cases where θ is varied, the
316 resulting cusps are saw-toothed shaped due to the asymmetry of the swash

317 trajectory. This is not seen in the cases where σ is varied, as the swash
318 trajectory is symmetrical about the shore normal. For increased σ , L_x tends
319 to slightly decrease while L_z and Δ remain fairly stable. For increased θ , L_x ,
320 L_z and Δ tend to increase.

321 *3.1.3. Series C: Time-varying wave conditions*

322 Case C1, run with measured wave data and the native sediment size of
323 0.5 mm, produced prominent cusp patterns with L_x and L_y equal to 3.8 and
324 19.2 m, respectively. Cusp patterns also emerge much earlier (after ~ 3 hours)
325 than the simulations with constant wave forcing (after ~ 18 hours), as the
326 wave conditions regularly changes with time. The beach cusps themselves are
327 also more dynamic, with greater long-shore migration observed in contrast to
328 relatively static cusps in the simulations with constant wave forcing. For the
329 remaining cases, cusps are either weakly defined (C2 and C4) or non-existent
330 (C3). For the latter (C3), the finer sediment size of 0.2 mm causes the beach
331 to strongly erode under the same wave conditions at case C1.

332 When the sediment size is decreased to 0.3 and 0.2 mm (cases C2 and C3,
333 respectively), the upper beach no longer accretes, but is rather eroded to form
334 a low tide terrace (wide shallow area around MSL in Figure 4 v-x). Cuspate
335 features can still be discerned for in the pattern of erosion for the case C2,
336 however the beach is featureless for case C3 as the wave conditions are highly
337 erosive for the fine sediment, resulting in a dissipative beach profile.

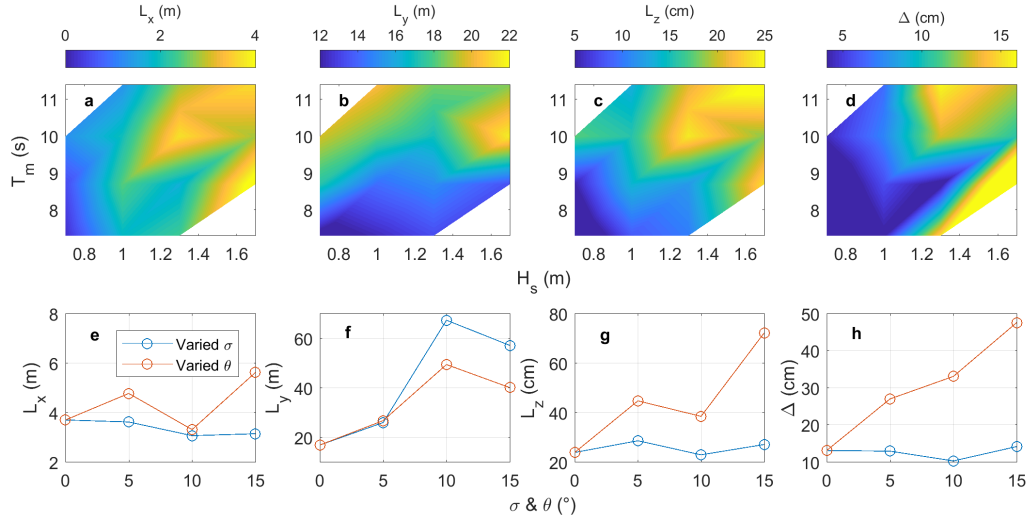


Figure 6: Resulting length scales of L_x , L_y , L_z and Δ for different combinations of wave conditions in the H_s - T_m parameter space (panels a-d) and, separately, in the σ and θ parameter space (panels e-h). Note that the legend in panel (e) also applies to panels (f-h).

338 3.2. Temporal Evolution and Swash Dynamics

339 3.2.1. Temporal development of cusps

340 Fig. 7 shows the temporal evolution of cusped morphology for the base
 341 case simulation (A10), which is fairly representative for all the other cases
 342 considered. During the initial rising tide, small alternating perturbations
 343 in the wave and current field are observed. The perturbations are, how-
 344 ever, too small cause any significant variation in $\langle \widetilde{H_{s,y}} \rangle$ or $\langle \widetilde{u_y} \rangle$, therefore
 345 the bathymetry is slow to respond. Nonetheless, during this initial period,
 346 sediment is slowly moved onshore, just below the tide level (Fig. 7f). This
 347 subaqueous mass of accreted sediment becomes exposed when the tide turns
 348 after the first high tide. It is reworked and sediment is freshly deposited at

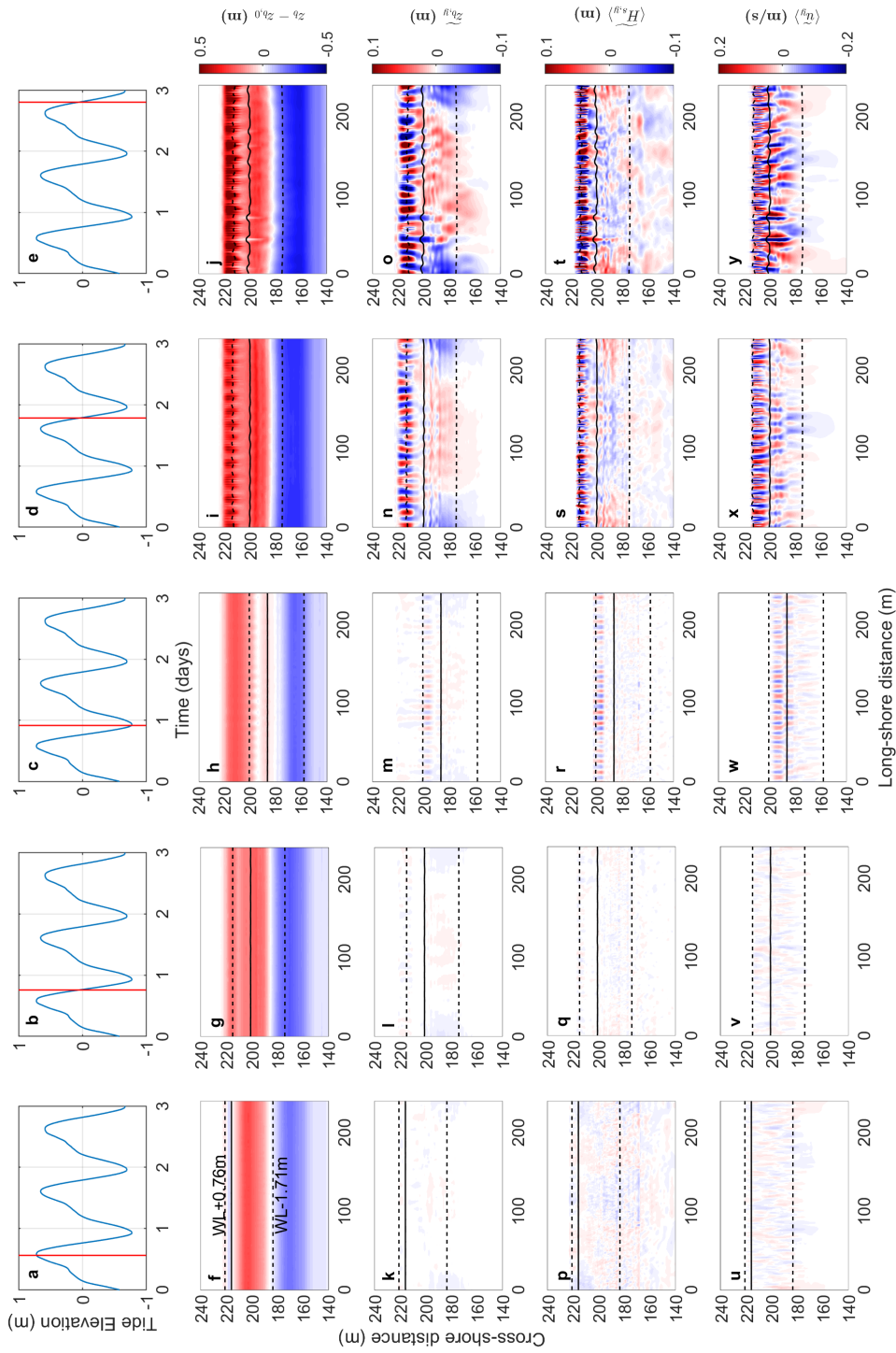


Figure 7: Temporal development of cusped morphology for the base case simulation (A10) shown during the first falling tide (high tide, mid-tide and low tide in columns 1-3, respectively) and for the last two mid-tides (columns 4-5). Rows 1 to 5 show the tide elevation, cumulative erosion/sedimentation pattern, $\langle \tilde{z}_{b,y} \rangle$, $\langle \tilde{H}_{s,y} \rangle$, and $\langle \tilde{u}_y \rangle$, respectively.

349 the top of the swash as the water level recedes, creating a berm (Fig. 7g).
 350 This trail of sediment is slowly sculpted into small cusped features as sed-
 351 iment deposition becomes irregular long-shore. By the start of the second
 352 tidal cycle, these remnant cusped perturbations, $\widetilde{z}_{b,y}$, begin to amplify the
 353 wave height pattern to a sufficient degree to cause notable variations in $\langle \widetilde{H}_{s,y} \rangle$
 354 and $\langle \widetilde{u}_y \rangle$, which further enhances $\widetilde{z}_{b,y}$ through positive feedback. Over time,
 355 these feedbacks allow the cusp dimensions to steadily increase over time,
 356 particularly L_x , L_z and Δ (as shown in Fig. 5).

357 For all simulations, the $\langle \widetilde{H}_{s,y} \rangle$ pattern is consistently negatively correlated
 358 with $\widetilde{z}_{b,y}$ ($-0.33 > r > -0.64$, averaged over last tidal cycle), with both
 359 patterns developing simultaneously. This indicates that wave heights are
 360 higher on the cusp horns and smaller in the troughs. Simulations in which
 361 the cusp field does not clearly materialize are those in which accretion is not
 362 particularly strong during the initial (and subsequent) tidal cycles, especially
 363 in the upper part of the beach. The cusp field also does not fully develop in
 364 simulations where the pattern of $\langle \widetilde{H}_{s,y} \rangle$ or $\langle \widetilde{u}_y \rangle$ is not strongly perturbed.

365 3.2.2. TKE and swash flow patterns

366 The variation of k along the central cross-shore transect allows us to see
 367 areas where wave-breaking-induced turbulence is strongest. The left panels in
 368 Fig. 8 show that k is maximum in the inner surf zone during the falling tide,
 369 maximum in the swash around high tide. Greater levels of swash turbulence
 370 around high tide (where cusps are to be found) is observed for increasing
 371 H_s , σ and θ . Swash flow patterns are generally found to be horn-divergent,
 372 with flow converging in the trough of the cusp with strong return currents
 373 (Fig. 8b and d). Flow patterns are elongated in swash for slightly increased

374 θ (case B4, Fig. 8f). The increased turbulence for small increases of σ and
375 θ beyond normal potentially amplifies cusp dimensions, but may prove to be
376 too dynamic for larger values above normal. Fig. 8g and h show, for case
377 B3, k values are consistently high in the surf and for longer periods in the
378 swash around high tide compared to the base case. The resulting mean flow
379 pattern lacks the rhythmicity observed in the base case, with more uniform
380 cross-shore flow.

381 3.2.3. Swash Excursion, Height and Slope

382 Fig. 9 shows S_x , S_z and β for the base case simulation, which has similar
383 results as most other cases. As seen in Fig. 9b, β and tide elevation are
384 positively correlated, varying at the same timescale (i.e., the beach is steeper
385 around high tide and more gently sloping around low tide). S_x is consistently
386 negatively correlated with the swash slope and tide elevation above MSL (i.e.,
387 S_x is smallest around high tide, where the beach slope is steepest). In some
388 cases, S_x is maximum at low tide while in others S_x is maximum just below
389 mid-tide and subsequently decreases towards low tide (Fig. 9c). The latter
390 is due to a berm forming at the low tide level that increases β around that
391 section of the beach profile. S_x and S_z increases, as expected, with increased
392 H_s . For the base case (A10), the swash excursion generally ranges between 6–
393 16 m; and for case C1 it ranges between 8–20m. At the end of the simulation,
394 S_x measures 9.5 m for case A10 and 13.9 m for case C1.

395 3.3. Surface Sediment Composition

396 The final simulation (case C4) shows the effect of varying the sediment
397 composition by including two classes of sediment (fine and coarse) in the

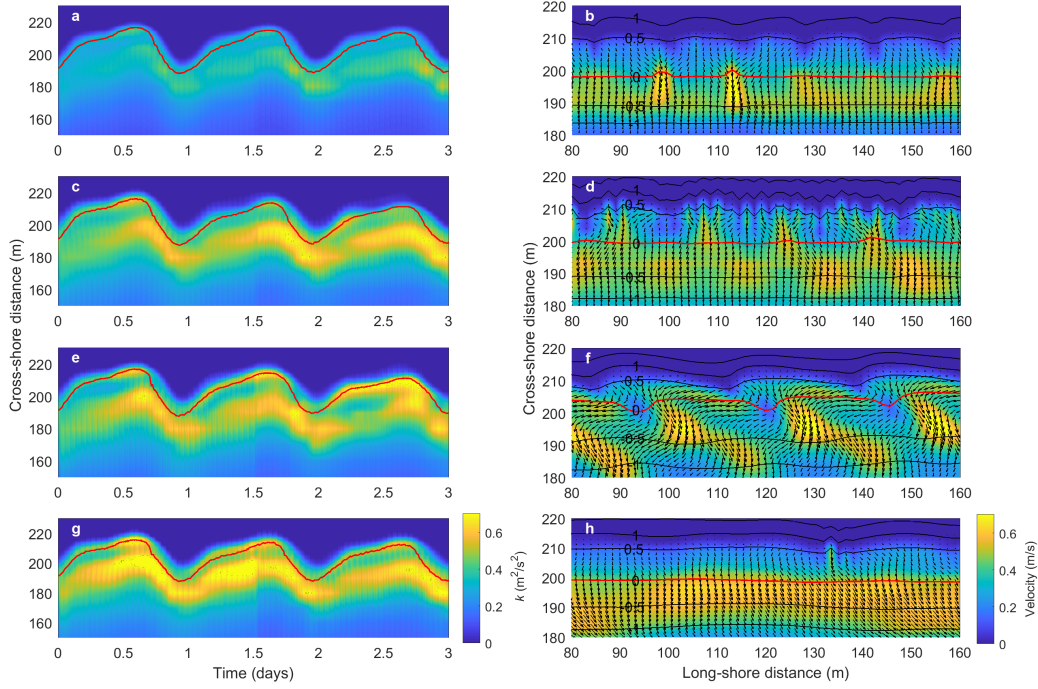


Figure 8: (Left panels) Temporal variation of turbulent kinetic energy (k) along the central cross-shore transect ($y = 120$ m) for cases A5, A10 (base case), B4 and B3 (panels a, c, e, and g, respectively). Red line indicates tide level. (Right panels) Spatial variation of the mean swash velocity field taken around the last mid-tide level ($T = 2.83$ days) for cases A5, A10 (base case), B4 and B3 (panels b, d, f, and h, respectively). Red line indicates shoreline (0 m contour level), and black lines show contour levels above and below spaced 0.5 m.

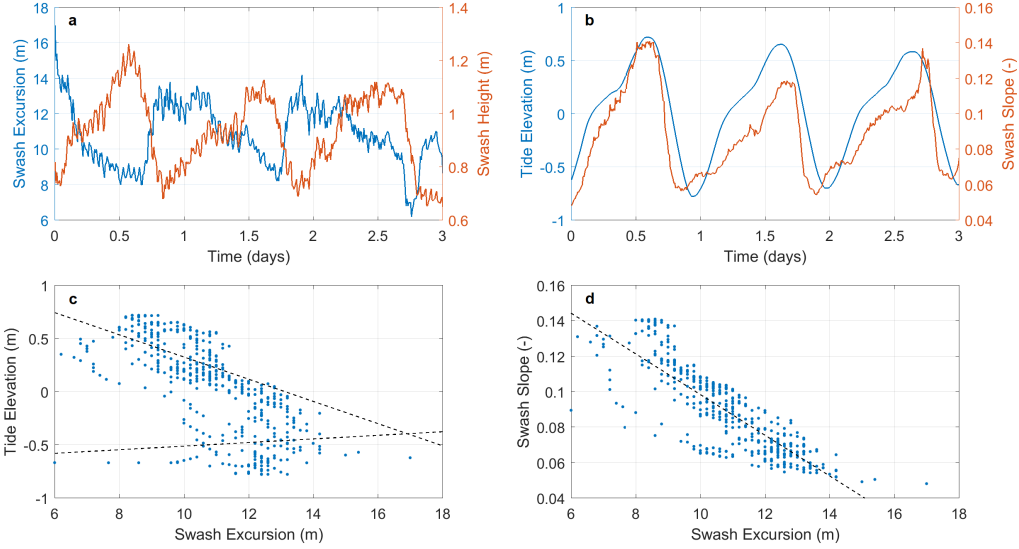


Figure 9: (Top panels) Temporal variation of swash excursion and swash height (a), and tide elevation and swash slope (b). (Bottom panels) Scatter plots of tide elevation (c) and swash slope (d) against swash excursion. Lines of best fit (black, dashed) are shown in (c) for data above and below -0.1 m tide elevation, and in (d) for all data.

398 surface and under layers. Both classes are equally distributed in the sedi-
 399 ment bed at the start of the simulation; however as time passes, the surface
 400 sediment composition ($P_{D_{50}}$) changes. The finer sediment fraction is gener-
 401 ally displaced from the swash zone and deposited on the low tide terrace
 402 while the coarser sediment fraction armours the swash (Fig. 10c-h). Despite
 403 this, there are still times when fine sediment will be pushed back into the
 404 surf zone during the rising tide (Fig. 10a); therefore, there is still a mixture
 405 of fine and coarse sediment in the surf zone over time. This mixture of fine
 406 and coarse sediment creates a pattern surrounding the cusp field with similar
 407 length scales as $\widetilde{z}_{b,y}$ (which identifies the cusp horns and troughs); therefore,
 408 it is possible investigate their long-shore correlation. This result is shown

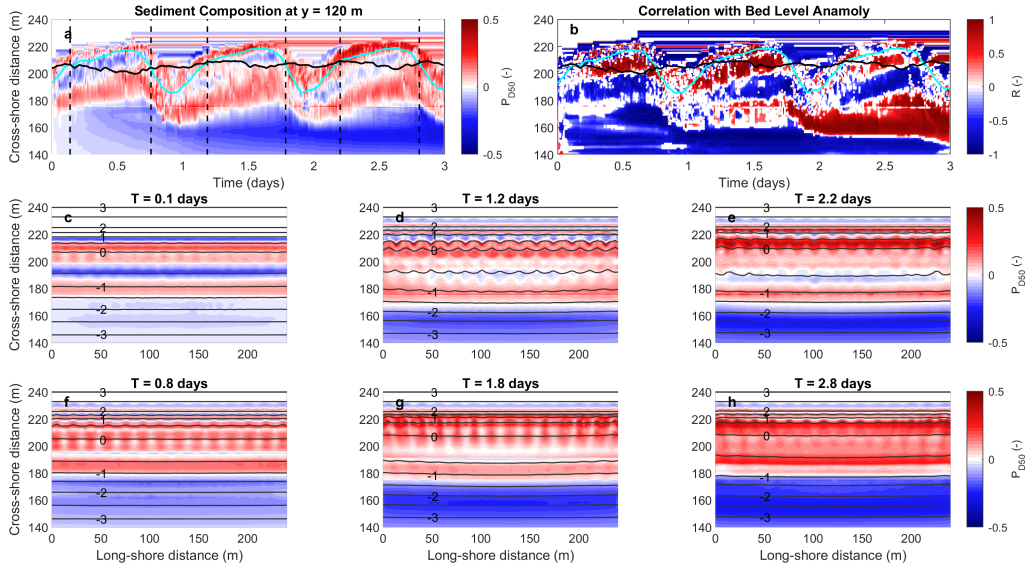


Figure 10: (a-b) Temporal evolution of (a) surface sediment composition ($P_{D_{50}}$) along the central cross-shore profile ($y = 120$ m), and (b) the correlation between $P_{D_{50}}$ and $\widetilde{z_{b,y}}$. Solid black and blue lines show the time-varying movement of the cross-shore position of the shoreline ($z = 0$ m) and the tide water level, respectively. (c-h) Spatial variation of $P_{D_{50}}$ at (c-e) mid-tide level on a rising tide and (f-h) mid-tide level on a falling tide. Dashed black lines in (a) indicate the times when (c-h) are shown. Black lines in (c-h) indicate bed level contours drawn at 0.5 m intervals. The colour scale in (a, c-h) is white (values near 0) for an evenly mixed bed (50% coarse and 50% fine sediment). Red colours (positive values up to 1) indicate a greater presence of coarser sediment, and vice versa for blue colours (negative values down to -1). Finally, the color scale in (b) is white (values near 0) when there is no correlation between $P_{D_{50}}$ and $\widetilde{z_{b,y}}$. Red colours indicate there is a positive correlation (coarser sediment located on cusp horn), and vice versa for blue colours (coarser sediment located in cusp trough).

409 in Fig. 10b, where temporal patterns of strong positive (and negative) cor-
 410 relations can be seen. Positive (negative) correlations shown in red (blue)
 411 indicate times when coarser sediment is found on the horn (trough) of the

412 cusps. The pattern of correlation fluctuates with tidal elevation but is gen-
413 erally positively correlated around the time-varying water level (i.e. coarser
414 sediment located on the horn). Nonetheless, there are times when the ex-
415 posed sediment composition pattern shows that coarser sediment is located
416 in the trough of the cusp rather than on the crest (e.g. the upper beach
417 during the second low tide).

418 4. Discussion

419 4.1. Evaluation of Length Scales

420 4.1.1. Comparison to Measurements at Nha Trang Beach

421 As we have used conditions representative of the situation at Nha Trang
422 Beach as the basis of our simulations, we therefore look to compare simulated
423 values of L_y to what was actually measured (28 m). Hardly any of the
424 cases in Series A come close, with mean L_y of 16.5 m. Even case C1, run
425 with measured H_s and T_m values, underestimates the measured value by
426 almost a third, with a final L_y of 19.2 m. However, it should be noted that
427 simulations in Series A and Series C are run with normally incident waves
428 without directional spreading. However, we have seen from Series B that
429 accounting for slight increases in σ and θ would result in larger values of L_y
430 (cases B1 and B4) that are more comparable to the measured value ($L_y > 26$
431 m). Simulated values of β in the base case and case C1 follow similar trends
432 as the measurements, being steepest around high tide and vice versa around
433 low tide. The range of simulated values are also around the same range as
434 the measurements, between 0.04 and 0.12. S_x tends to be maximum at low
435 tide in the simulations (where β is lowest) while, on the other hand, it is

436 maximum around high tide in the measured data (where β is highest).

437 If we consider the average wave conditions (defined by H_s and T_m) for
438 case C1 during the 3-day simulation period (approximately 1.17m and 10 s,
439 respectively), it would fall between the time-constant forcing values of case
440 A6 and A10. Wave conditions peaked during the first tide cycle (1.4 m and
441 11.5 s, similar to case A11), and were lowest during the last tidal cycle (1.0
442 m and 8.5 s, similar to case A5). The cusps produced at the end of the
443 simulation in C1 are of similar magnitude as case A6, A10 and A11 (mid-
444 to high-end of the wave conditions). After being formed during the first tide
445 cycle, L_y did not adapt to the smaller dimensions expected during the lower
446 energy conditions (shown for case A5). Instead, L_y remains fairly constant
447 as energy levels fall, as also observed in the field. Thus, the sequencing of
448 wave conditions can affect resultant cusp spacing, as commonly noted in the
449 field where pre-existing cusp formations may persist for some time before
450 newer cusp fields are able to develop, largely depending on how quickly and
451 to what degree actual wave conditions change (van Gaalen et al., 2011).

452 Finally, we note that L_y does not vary significantly between high and
453 mid-tide in our simulations or from the observations at Nha Trang Beach,
454 perhaps due to the micro-tidal environment. Nolan et al. (1999) were able
455 to show a dependence of L_y on elevation above MSL; however, their study
456 site was located in a meso-tidal environment (2.6 m range) exposed to more
457 energetic wave conditions.

458 *4.1.2. Comparison to Empirical and Theoretical Formulae*

459 Empirical equations for predicting L_y have been developed based on field
460 observations. Once such by Sunamura (2004) uses the sediment diameter

461 (D_{50}), wave period, wave height, and gravitational acceleration (g) as depen-
 462 dent variables, given as:

$$L_{y,Sun} = Aexp(-0.23D_{50}^{0.55})T\sqrt{gH} \quad (5)$$

463 where A is a scaling factor ranging from ~ 0.65 for laboratory cases to ~ 1.35
 464 for field cases. Expected values of L_y may also be calculated based on both
 465 the self-organisation and edge wave generation theories, shown, respectively,
 466 in Eq. 6 and Eq. 7 following as:

$$L_{y,SO} = fS_x \quad (6)$$

$$L_{y,EW} = \frac{gT_i^2}{m\pi} \sin\beta \quad (7)$$

467 where f is a factor generally taken to be 1.63 (but which may range between
 468 1 and 3); S_x is the swash excursion; m is a factor equal to 1 and 2 for sub-
 469 harmonic ($L_{y,Sub}$) and synchronous ($L_{y,Syn}$) edge waves, respectively; β is the
 470 beach slope; and T_i is the incoming wave period (Coco et al., 1999). Results
 471 are shown in Table 4 for final values of S_x (extracted from the model output
 472 around $T = 2.83$ days), from which final values of β and f are computed.
 473 Values of $L_{y,Sub}$, $L_{y,Syn}$, $L_{y,SO}$, and $L_{y,Sun}$ are also shown for comparison
 474 with Series A. It should be noted that some scatter is expected in our data
 475 as we are unable to control exactly where along a cusp (between the horn
 476 and trough) S_x and β are extracted, as the exact position of cusps at the
 477 central cross-shore profile varies during the course of the simulation for each
 478 case.

479 When using Eq. 5 to compute $L_{y,Sun}$ in Table 4, we computed and used
 480 the value of A that minimised the root-mean-square error (the best-fit value)
 481 between $L_{y,Sun}$ and L_y , which was equal to 0.6 – very close to the value of
 482 0.65 reported in Sunamura (2004). Values of $L_{y,Sun}$ are not much different
 483 to the simulation results of Series A, with raw error around 14% on average.
 484 Applying Eq. 5 to the average measured wave conditions (1 m, 9 s) and
 485 using the field value of $A = 1.35$, we obtain a predicted value of $L_{y,Sun}$ of
 486 32 m, a slight over-prediction. Thus, Eq. 5 predicts L_y reasonably well for
 487 both Series A (laboratory-type cases which have no directional spreading
 488 and normally incident waves) and for the actual field case at Nha Trang
 489 Beach. For Series B, where θ and σ are increased, using $A = 0.6$ largely
 490 underestimates L_y . The estimate is improved when using $A = 1.35$, with
 491 a best-fit value of 1.7. Sunamura (2004) noted the large difference between
 492 A obtained for laboratory and field data, attributing the larger field value
 493 to irregular wave forcing in the field. However, it should also be noted that
 494 slight increases in θ and σ in Series B also enhanced L_y , which may also help
 495 to account for the larger A values of field cases, since there is at least some
 496 degree of directional spreading expected.

497 Table 4 shows that simulated β and f generally increase with H_s and T_m .
 498 With regard to f , the simulation results ranges from 1.16 to 2.47, which fits
 499 within the range of expected f values (1 to 3). The best-fit value of f is
 500 found to be 1.63 – equal to that reported in Coco et al. (1999). As f varies
 501 according to specific forcing conditions, values of $L_{y,SO}$ overestimate L_y at
 502 low H_s and T_m values (such as case A1 or A4) and vice versa at high H_s and
 503 T_m values (such as case A11 or A14). Almar et al. (2008) and Vousdoukas

504 (2012) have reported observed mean f values of 1.69 and 3.47, respectively,
 505 under average wave conditions of $[H_s, T_m] = [1.5 \text{ m}, 10 \text{ s}]$ at Tairua Beach
 506 (former), and $= [1 \text{ m}, 8 \text{ s}]$ at Faro Beach (latter). While the observed f -value
 507 of Almar et al. (2008) is not much different with our findings from Series A
 508 (θ is reported to be almost always shore normal), that of Vousdoukas (2012)
 509 is much larger than expected. For the latter, it is important to note that
 510 there were large variations of measured θ values, up to 40° . This may help to
 511 explain why the observed L_y (on average 50 m) is quite large in comparison
 512 to the measured S_x . As seen from our simulations, for $\theta \geq 10^\circ$ (cases B5
 513 and B6) we obtain mean f values of 5.8 and L_y of 45 m – comparable to
 514 Vousdoukas (2012).

515 Regarding the synchronous edge wave theory, $L_{y, syn}$ significantly underes-
 516 timates L_y for cases with lower H_s and T_m values (for cases A1–A5, around
 517 48% lower) and vice versa at high H_s and T_m values (for cases A10–A14,
 518 around 12% higher). Alternatively, for sub-harmonic edge waves, $L_{y, sub}$
 519 slightly overestimates L_y for cases with lower H_s and T_m values (for cases
 520 A1–A5, around 5% lower) but severely overestimates L_y at high H_s and
 521 T_m values (for cases A10–A14, around 125% higher). Similar findings are
 522 shown in Dodd et al. (2008), though only T_m was varied in their simulations.
 523 Therefore, $L_{y, sub}$ predictions would appear to be suited to low wave energy
 524 conditions and those for $L_{y, syn}$ to higher energy conditions; but neither are
 525 very good predictors across the board when compared to L_y . Guza and In-
 526 man (1975) note that sub-harmonic edge waves are more easily generated
 527 than synchronous edge waves, and that both are not generally found under
 528 energetic wave conditions, where the high turbulence of plunging breakers

529 disrupts their excitation. The generation of certain types of edge waves in
530 itself is also highly dependent on, *inter alia*, beach topography, frequency
531 spread of incident waves, and dissipation by waves and currents. Therefore
532 it is not clear which edge wave mode is best suited for comparison to L_y .
533 Indeed in the literature, comparisons between measured data and theoretical
534 edge wave predictions vary widely from being strongly to weakly correlated
535 (Kaneko, 1985; Rasch et al., 1993; Almar et al., 2008) and even distinguishing
536 between different modes of edge waves may be difficult in reality (Holland
537 and Holman, 1996). Nevertheless, it may be possible to identify edge waves
538 using XBeach (whether synchronous or sub-harmonic) from seaward radiat-
539 ing wave reflection patterns. As shown in Fig. 7, a pattern of alternating
540 perturbations in $\langle \widetilde{H_{s,y}} \rangle$ is seen during the initial development of cusps, obvi-
541 ously caused by the interaction between incoming and reflected waves (similar
542 to Almar et al. (2018)). However, our model output is not saved at a high
543 enough frequency to separate incoming from reflected waves, and we are thus
544 unable to definitively quantify the presence of edge waves. Nonetheless, this
545 may be looked at in greater detail in future work that is more focused on
546 mechanisms surrounding cusp initiation.

547 4.2. Evaluation of development, circulation and sediment patterns

548 We have shown in our simulations that increased T_m generally results in
549 increased L_y . Longer intervals between swash events for higher period waves
550 would tend to reduce bore (swash-swash) interactions occurring on the beach-
551 face, allowing stronger return flow during the backwash capable of sculpting
552 wider cusps. Dodd et al. (2008) obtained similar results, and showed that
553 the swash period may resonate with the incoming wave period to enhance

Run ID	S_x (m)	β (-)	f (-)	L_y (m)	$L_{y,Sub}$ (m)	$L_{y,Syn}$ (m)	$L_{y,SO}$ (m)	$L_{y,Sun}$ (m)
A1	9.8	0.044	1.16	11.4	10.2	5.1	16.0	9.8
A2	9.3	0.052	1.85	17.3	17.1	8.5	15.2	11.7
A3	8.5	0.055	2.29	19.6	24.0	12.0	13.9	13.4
A4	10.0	0.055	1.23	12.3	12.7	6.3	16.3	11.7
A5	12.0	0.048	1.18	14.2	15.9	8.0	19.6	14.0
A6	8.3	0.071	2.19	18.2	30.7	15.4	13.6	16.1
A7	8.2	0.078	2.47	20.3	44.1	22.1	13.4	18.3
A8	11.4	0.056	1.17	13.3	13.0	6.5	18.5	13.4
A9	9.6	0.072	1.56	15.0	23.8	11.9	15.7	15.9
A10	9.5	0.075	1.80	17.0	32.5	16.2	15.4	18.3
A11	8.5	0.094	2.17	18.5	53.2	26.6	13.9	20.9
A12	9.9	0.081	1.36	13.4	26.8	13.4	16.1	18.2
A13	12.2	0.083	1.77	21.6	36.1	18.0	19.8	20.9
A14	11.1	0.092	1.69	18.7	51.9	25.9	18.0	23.9
B1	12.5	0.066	2.08	26.1	–	–	–	–
B2	11.9	0.064	5.66	67.4	–	–	–	–
B3	13.9	0.061	4.12	57.3	–	–	–	–
B4	8.1	0.115	3.33	26.9	–	–	–	–
B5	7.3	0.098	6.79	49.5	–	–	–	–
B6	8.4	0.096	4.80	40.2	–	–	–	–
C1	13.9	0.059	1.39	19.2	–	–	–	–
C2	13.5	0.060	1.48	20.0	–	–	–	–
C3	13.2	0.063	2.10	27.7	–	–	–	–
C4	14.9	0.083	1.29	19.3	–	–	–	–

Table 4: Simulation results of S_x , β , f and L_y for Series A, B and C, with Series A compared with expectations from the edge wave (sub-harmonic and synchronous) and self-organisation theories, and Sunamura (2004) ($L_{y,Sub}$, $L_{y,Syn}$, $L_{y,SO}$ and $L_{y,Sun}$, respectively).

554 backwash. Our simulations also showed that increased H_s leads to larger
555 L_x and L_z , most likely caused by greater turbulence in the swash capable
556 of reworking sediment into deeper and wider cusp features. All simulations
557 with developed cusps featured horn-divergent flow patterns, as is commonly
558 observed in the field (Masselink and Pattiaratchi, 1998b; Holland, 1998) and
559 predicted by other numerical studies (Dodd et al., 2008).

560 Cusp dimensions are enhanced when σ (under normally incident waves)
561 or θ are low ($\sim 5^\circ$). Larger values are shown to cause increased turbulence in
562 the swash, which acts to inhibit cusp growth. Increased turbulence may be
563 due to the effect of greater swash-swash interactions ($\sigma > 0$) or asymmetric
564 swash flow ($\theta > 0$). Obliquely incident waves of 20° have been observed
565 in the field to flatten cusped features (Masselink and Pattiaratchi, 1998a).
566 Holland (1998) also noted that cusps are rarely observed, and tend to be
567 destroyed, for angles of incidence greater than 12° . Holland (1998) suggests
568 that as θ increases, long-shore currents increasingly disrupt the cross-shore
569 flow structure needed to form and maintain cusps. In our simulations where
570 θ is varied, only case B4 resulted in a prominent cusp shape. While B5 and
571 B6 do produce shoreline undulations, they have high aspect ratios which
572 diminish their prominence.

573 In terms of the sediment sorting pattern around cusps, by looking at the
574 correlation between $P_{D_{50}}$ and $\widetilde{z}_{b,y}$ in Fig. 10b, we showed that sediment is
575 generally coarser on the horns than in the trough of the cusps. This is true
576 for most field observations, such as Antia (1987) and Sallenger (1979) who
577 also explains that, as swash flow is more powerful than backwash and as flow
578 is generally horn divergent, fine sediment is removed from the horn (leaving

579 coarser sediment behind) and deposited in the trough.

580 The effect of varying sediment size, by decreasing D_{50} , we obtain slight
581 increases in L_y , as noted in Sunamura (2004). However, it comes at the
582 expense of increasing the erodability of the beach (i.e. more dissipative),
583 making cusps less prominent. In fact, case C3 the final profile is generally
584 devoid of any shoreline features. The present results therefore show cusps
585 tend to form under accretive and mildly erosive conditions on coarse grained
586 intermediate beaches, consistent with field observations (Holland, 1998; van
587 Gaalen et al., 2011). Antia (1987) notes that while cusps may form on typ-
588 ically dissipative beaches, they only appear during low energy events which
589 may permit a temporary reflective beach state to form.

590 *4.3. XBeach Sediment Transport Module*

591 The simulations have been done using the non-hydrostatic wave solver
592 in XBeach while enabling sediment transport. This is quite experimental,
593 as the sediment transport equations only account for transport due to flow
594 and wave-averaged orbital motions and therefore do not resolve intra-wave
595 transport mechanisms. Furthermore, the use of the parameter settings in
596 Table 1 with the Kingsday version of XBeach allows bedload transport to be
597 only onshore-directed, which is an unusual result that is repaired in subse-
598 quent model releases. Nonetheless, an appropriate balance between onshore
599 and offshore transport fluxes are obtained for our simulations despite these
600 shortcomings. Further development of XBeach is therefore necessary to bet-
601 ter and more realistically account for intra-wave and swash sediment trans-
602 port processes. One suggestion to the model developers may be, for exam-
603 ple, introducing acceleration dependent onshore fluxes as can be determined

604 from gradients in the surface elevation computed by the non-hydrostatic wave
605 solver.

606 5. Conclusion

607 A number of exploratory morphodynamic simulations were carried out to
608 study beach cusp formation, inspired by observations at Nha Trang Beach,
609 Vietnam. The simulations used time-constant and time-varying (measured)
610 wave forcing conditions. In the former, the length scale of cusp formations
611 were analysed as a function of the significant wave height, mean wave period,
612 directional spreading and angle of incidence (H_s , T_m , σ and θ , respectively).
613 The resulting cusp length scales varied according to well-established norms
614 – H_s modulates cusp height and cross-shore depth, while T_m , σ and θ af-
615 fect long-shore length scales. Cusps appear to be most prominent for longer
616 period waves (> 10 s) with moderate wave heights (> 1.3 m). Slightly in-
617 creased σ and θ enhances long-shore length scales, but tends to make cusps
618 less prominent at values $> 10^\circ$. The model was able to produce asymmetric
619 cusp patterns for obliquely incident waves.

620 Time-varying (measured) wave conditions with the native sediment size
621 produced cusps with smaller length scales to those measured; however, it may
622 be possible to achieve a more comparable spacing by including directional
623 variations. Reducing the median sediment diameter, D_{50} , in other simu-
624 lations with time-varying wave conditions allowed more dissipative beach
625 profiles to form, resulting in net erosion of the beachface (as opposed to ac-
626 cretion in the previous simulations). Cusps were able to form under mildly
627 erosive conditions (using $D_{50} = 0.3$ mm), though not as prominent as when

628 formed under accretive conditions. Cusps were not able to form under more
629 intense erosion (using $D_{50} = 0.2$ mm). This finding is in keeping with the
630 many observations of cusps being found on coarse sand beaches rather than
631 fine sand beaches. The model also showed a general tendency for coarse
632 sediment to be located on the crest of cusps near the water line, though the
633 inverse pattern was seen at other elevations on the beach face.

634 Given that the model is able to reasonably simulate the formation of
635 cusps of varying length scales and prominence, the process of cusp initiation
636 can be studied in more detail in future work. Initial results show there is
637 a significant correlation between the long-shore wave height and bed level
638 anomalies, which may be produced by wave reflection patterns as suggested
639 in Almar et al. (2018). It is currently unknown to what extent edge waves
640 play a role in cusp formation; however, this study provides a basis for more
641 rigorous investigation of this enigmatic topic using the XBeach model.

642 **Acknowledgements**

643 This research has received support from French grants through ANR
644 (COASTVAR: ANR-14-ASTR-0019) and CG29 subvention. The authors
645 would like to thank all the participants present in the Nha Trang field exper-
646 iment for the help provided. CD acknowledges the Conseil Départemental
647 du Finistère, LabexMer (ANR-10-LABX-19), and the Marie Curie Prestige
648 Fellowship Program for providing financial support for his postdoctoral re-
649 search at UBO. CD also acknowledges Jaap Nienhuis and NSF Award No.
650 1810855 for support during his postdoctoral stay at Florida State University.
651 The authors thank Giovanni Coco and two other anonymous reviewers for

652 their detailed comments and feedback, which greatly helped to improve the
653 quality of the manuscript.

654 **Author Contributions**

655 FF, RA and LPA designed and carried out the field campaign and in-situ
656 data collection at Nha Trang beach. MJ produced the orthophoto beach
657 DEM from the drone measurements. CD designed and performed the model
658 simulations, post-processed measured data, analysed the model results and
659 produced the figures. The manuscript was written and revised by CD, with
660 comments from other co-authors.

661 **Conflicts of Interest**

662 The authors declare no conflict of interest.

663 **References**

- 664 Almar, R., Coco, G., Bryan, K., Huntley, D., Short, A., Senechal, N., 2008.
665 Video observations of beach cusp morphodynamics. *Marine Geology* 254,
666 216–223.
- 667 Almar, R., Lerma, A.N., Castelle, B., Scott, T., 2018. On the influence
668 of reflection over a rhythmic swash zone on surf zone dynamics. *Ocean*
669 *Dynamics* 68, 899–909.
- 670 Almeida, L.P., Almar, R., Blenkinsopp, C., Senechal, N., Bergsma, E.,
671 Floc’h, F., Caulet, C., Biauxque, M., Marchesiello, P., Grandjean, P., Am-
672 mann, J., Benschila, R., Thuan, D.H., Gomes da Silva, P., Viet, N.T.,

- 673 2020. Lidar observations of the swash zone of a low-tide terraced trop-
674 ical beach under variable wave conditions: The nha trang (vietnam)
675 coastvar experiment. *Journal of Marine Science and Engineering* 8, 302.
676 doi:doi:10.3390/jmse8050302.
- 677 Antia, E., 1987. Preliminary field observations on beach cusp formation and
678 characteristics on tidally and morphodynamically distinct beaches on the
679 nigerian coast. *Marine Geology* 78, 23–33.
- 680 Bakhtyar, R., Barry, D., Jeng, D., Li, L., Yeganeh-Bakhtiary, A., 2009. Mod-
681 eling sediment transport in the swash zone: A review. *Ocean Engineering*
682 36, 767–783.
- 683 de Bakker, A., Tissier, M., Ruessink, B., 2014. Shoreline dissipation of in-
684 fragravity waves. *Continental Shelf Research* 72, 73–82.
- 685 Coco, G., Burnet, T., Werner, B., Elgar, S., 2003. Test of self-organization
686 in beach cusp formation. *J. Geophys. Res* 108, 3101.
- 687 Coco, G., Huntley, D., O’Hare, T., 2000. Investigation of a self-organization
688 model for beach cusp formation and development. *Journal of Coastal*
689 *Research* 105, 21991–22002.
- 690 Coco, G., Huntley, D., O’Hare, T., 2001. Regularity and randomness in the
691 formation of beach cusps. *Marine Geology* 178, 1–9.
- 692 Coco, G., O’Hare, T., Huntley, D., 1999. Beach cusps: a comparison of data
693 and theories for their formation. *Journal of Coastal Research* 15, 741–749.

- 694 Daly, C., Floc'h, F., Almeida, L.P., Almar, R., 2017. Modelling accretion at
695 nha trang beach, vietnam. Proceedings of the International Conference on
696 Coastal Dynamics, Helsingor, Denmark , 1886–1896.
- 697 Dodd, N., Stoker, A., Calvete, D., Sriariyawat, A., 2008. On beach cusp
698 formation. *Journal of Fluid Mechanics* 597, 145–169.
- 699 Elgar, S., Gallagher, E., Guza, R., 2001. Nearshore sandbar migration. *Jour-
700 nal of Geophysical Research* 106, 11623–11627.
- 701 van Gaalen, J., Kruse, S., Coco, G., Collins, L., Doering, T., 2011. Observa-
702 tions of beach cusp evolution at melbourne beach, florida, usa. *Geomor-
703 phology* 129.
- 704 Garnier, R., Ortega-Sanchez, M., Losada, M., Falques, A., Dodd, N., 2010.
705 Beach cusps and inner surf zone processes: growth or destruction? a
706 case study of trafilgar beach (cadiz, spain). *Scientia Marina* 74, 539–553.
707 doi:10.3989/scimar.2010.74n3539.
- 708 Guza, R., Inman, D., 1975. Edge waves and beach cusps. *Journal of Geo-
709 physical Research: Oceans and Atmosphere* 80, 2997–3012.
- 710 Holland, K., 1998. Beach cusp formation and spacings at duck, usa. *Conti-
711 nental Shelf Research* 18, 1081–1098.
- 712 Holland, K., Holman, R., 1996. Field observations of beach cusps and swash
713 motions. *Marine Geology* 134, 77–93.
- 714 Inman, D., Guza, R., 1982. The origin of swash cusps on beaches. *Marine
715 Geology* 49, 133–148.

- 716 Kaneko, A., 1985. Formation of beach cusps in a wave tank. *Coastal Engi-*
717 *neering* 9, 81–98.
- 718 Lashley, C.H., Roelvink, D., van Dongeren, A., Buckley, M.L., Lowe, R.J.,
719 2018. Nonhydrostatic and surfbeat model predictions of extreme wave
720 run-up in fringing reef environments. *Coastal Engineering* 137, 11–27.
- 721 Masselink, G., Hegge, B.J., Pattiaratchi, C.B., 1997. Beach cusp morphody-
722 namics. *Earth Surface Processes and Landforms* 22, 1139–1155.
- 723 Masselink, G., Pattiaratchi, C., 1998a. Morphodynamic impact of sea breeze
724 activity on a beach with beach cusp morphology. *Journal of Coastal Re-*
725 *search* 14, 393–406.
- 726 Masselink, G., Pattiaratchi, C., 1998b. Morphological evolution of beach
727 cusps and associated swash circulation patterns. *Marine Geology* 146,
728 93–113.
- 729 McCall, R., Masselink, G., Roelvink, J., Russell, P., Davidson, M., Poate, T.,
730 2012. Modeling overwash and infiltration on gravel barriers. *Proceedings*
731 *of the 33rd International Conference on Coastal Engineering, Santander,*
732 *Spain .*
- 733 Nolan, T., Kirka, R., Shulmeister, J., 1999. Beach cusp morphology on sand
734 and mixed sand and gravel beaches, south island, new zealand. *Marine*
735 *Geology* 157, 185–198.
- 736 O’Dea, A., Brodie, K., 2019. Spectral analysis of beach cusp evolution using
737 3d lidar scans. *Proceedings of the 9th International Conference on Coastal*
738 *Sediments, Tampa/St. Petersburg, Florida, World Scientific , 657–673.*

- 739 Rasch, M., Nielsen, J., Nielsen, N., 1993. Variations of spacings between
740 beach cusps discussed in relation to edge wave theory. *Geografisk Tidsskrift*
741 - Danish Journal of Geography 93, 49–55.
- 742 van Rhee, C., 2010. Sediment entrainment at high flow velocity. *Journal of*
743 *Hydraulic Engineering* 136, 572–582.
- 744 van Rijn, L., 2007a. Unified view of sediment transport by currents and
745 waves. i: initiation of motion, bed roughness, and bed-load transport.
746 *Journal of Hydraulic Engineering* 133, 649–667.
- 747 van Rijn, L., 2007b. Unified view of sediment transport by currents and
748 waves. ii: suspended transport. *Journal of Hydraulic Engineering* 133,
749 668–689.
- 750 Roelvink, D., van Dongeren, A., McCall, R., Hoonhout, B., van Rooijen,
751 A., van Geer, P., de Vet, L., Nederhoff, K., Quataert, E., 2015. Xbeach
752 technical reference: Kingsday release model description and reference guide
753 to functionalities. Deltares, UNESCO-IHE Institute of Water Education
754 and Delft University of Technology .
- 755 Roelvink, D., van Dongeren, A., McCall, R., Hoonhout, B., van Rooijen,
756 A., van Geer, P., de Vet, L., Nederhoff, K., Quataert, E., 2018. Im-
757 proving predictions of swash dynamics in xbeach: The role of groupi-
758 ness and incident-band runup. *Coastal Engineering* 134, 103–123.
759 doi:doi.org/10.1016/j.coastaleng.2017.07.004.
- 760 Roelvink, D., Reniers, A., van Dongeren, A., van Thiel de Vries, J., McCall,

- 761 R., Lescinski, J., 2009. Modelling storm impacts on beaches, dunes and
762 barrier islands. *Coastal Engineering* 56, 1133–1152.
- 763 Ruessink, B., Ramaekers, G., van Rijn, L., 2012. On the parameterization
764 of the free-stream non-linear wave orbital motion in nearshore morphody-
765 namic models. *Coastal Engineering* 65, 56–63.
- 766 Ruffini, G., Briganti, R., Alsina, J.M., Brocchini, M., 2020. Nu-
767 merical modeling of flow and bed evolution of bichromatic wave
768 groups on an intermediate beach using nonhydrostatic xbeach. *Jour-
769 nal of Waterway, Port, Coastal, and Ocean Engineering* 146.
770 doi:doi.org/10.1061/(ASCE)WW.1943-5460.0000530.
- 771 Sallenger, A., 1979. Beach cusp formation. *Marine Geology* 29, 23–37.
- 772 Soulsby, R., 1997. Dynamics of marine sands: a manual for practical appli-
773 cations. Thomas Telford Publications, London.
- 774 Sunamura, T., 2004. A predictive relationship for the spacing of beach cusps
775 in nature. *Coastal Engineering* 51, 697–711.
- 776 Talmon, A., van Mierlo, M., Struiksmā, N., 1995. Laboratory measurements
777 of the direction of sediment transport on transverse alluvial-bed slopes.
778 *Journal of Hydraulic Research* 33, 495–517.
- 779 Vousdoukas, M., 2012. Erosion/accretion patterns and multiple beach cusp
780 systems on a meso-tidal steeply-sloping beach. *Geomorphology* 141-142,
781 34–46.

- 782 Walstra, D., van Rijn, L., van Ormondt, M., Briere, C., Talmon, A.M.,
783 2007. The effects of bed slope and wave skewness on sediment transport
784 and morphology. Proceedings of the Sixth International Symposium on
785 Coastal Sediments, ASCE , 137–150.
- 786 van der Werf, J., Ribberink, J., Kranenburg, W., Neessen, K., Boers, M.,
787 2017. Contributions to the wave-mean momentum balance in the surf
788 zone. Coastal Engineering 121, 212–220.
- 789 Werner, B., Fink, T., 1993. Beach cusps as self-organized patterns. Science
790 260, 968–971.
- 791 Zijlema, M., Stelling, G.S., Smit, P.B., 2011. Swash: An operational public
792 domain code for simulating wave fields and rapidly varied flows in coastal
793 waters. Coastal Engineering 58, 992–1012.